Geoscience Frontiers 16 (2025) 101940

Contents lists available at ScienceDirect

Geoscience Frontiers

journal homepage: www.elsevier.com/locate/gsf

Research Paper

# Stability and physical properties of brucite at high pressures and temperatures: Implication for Earth's deep water cycle

Ningyu Sun [a], Xinyang Li [b], Luo Li [a], Qingchun Zhang [a], Yingxin Yu [a], Zhu Mao [a,c,*], Cijin Zhou [a], Dongzhou Zhang [d]

[a] *Deep Space Exploration Laboratory/School of Earth and Space Sciences, University of Science and Technology of China, Hefei 230026, PR China*
[b] *State Key Laboratory of Superhard Materials, Jilin University, Changchun 130012, PR China*
[c] *CAS Center for Excellence in Comparative Planetology, University of Science and Technology of China, Hefei 230026, Anhui, PR China*
[d] *Center for Advanced Radiation Sources, University of Chicago, Chicago, IL 60637, USA*

## ARTICLE INFO

*Article history:*
Received 7 April 2024
Revised 1 July 2024
Accepted 27 September 2024
Available online 2 October 2024

*Keywords:*
Brucite
Phase stability
High pressure–temperature
Subducted slabs
Hydrous harzburgite

## ABSTRACT

Brucite is a common hydrous mineral on Earth and may contribute to the deep water cycle of the Earth, but its stability and structure under mantle conditions remain uncertain. In this study, we investigated the stability of brucite up to 60 GPa at 800 K and 45 GPa at 1850 K. Within the experiment *P-T* conditions, no theoretically predicted new phase was observed, and brucite remained in the $P\bar{3}m1$ structure. With the determined thermal EoS of brucite and the elastic parameters of mantle minerals, we modeled the velocity and density profile of subducted hydrous harzburgite in the top lower mantle, assuming that the water was stored in brucite and phase D. Based on the modelling, 1 wt.% water will reduce the velocity and density of harzburgite by ~ 5% and ~ 2%, respectively, yet whether the water is stored in brucite or phase D has weak influence on both density and velocity. With a water content up to 2.4 wt.%, the density of hydrous harzburgite could be reduced to 2.2(2)%–2.8(2)% lower than the surrounding mantle, while the $V_P$ and $V_S$ of hydrous harzburgite are still 0.3(1)%–0.7(1)% and 0.7(2)%–1.8(2)% higher than that of the normal mantle. Thus, the low-density hydrous harzburgite may slow down the subducting of slab, despite being a high-velocity body in seismic observations.

## 1. Introduction

Petrological studies have discovered the presence of hydrous ringwoodite and ice VII as diamond inclusions originating from the bottom transition zone or even the top lower mantle in various locations of the Earth, indicating that at least some regions of the Earth's mantle could be very hydrous (Pearson et al., 2014; Tschauner et al., 2018). Since most hydrous minerals in the sinking slabs will dehydrate continuously with increasing depth, only a few, such as dense hydrous magnesium silicates (DHMSs), δ-AlOOH, and $Fe_2OH_x$, which were formed by a succession of phase transitions, may survive at relevant pressure–temperature (*P-T*) conditions of the Earth's transition zone and lower mantle (e.g. Litasov et al., 2007; Litasov et al., 2008; Nishi et al., 2014; Li et al., 2016; Duan et al., 2018; Liu et al., 2019; Ohtani, 2020; Piet et al., 2020). Searching for stable hydrous minerals/phases at relevant *P-T* conditions of the Earth's lower mantle is thus critical to understanding the transportation and circulation of water in the Earth's deeper interior.

Brucite, [$Mg(OH)_2$], is the simplest hydrous mineral in the MgO-$SiO_2$-$H_2O$ (MSH) system containing 30.8 wt.% water (50 mol.%) (Fig. 1) (Walter et al., 2015). The stability of brucite at relevant *P-T* conditions of the mantle has attracted extensive research interest over decades (e.g. Fei and Mao, 1993; Duffy et al., 1995; Fukui et al., 2005; Guo, 2016). Brucite crystalizes in the trigonal structure with the space group $P\bar{3}m1$ under ambient conditions, while it was theoretically predicted to change into the $P\bar{3}$-phase and $P4_12_12$ structure under high pressure (Hermann and Mookherjee, 2016). Of particular interest is the new $P4_12_12$ structure (Hermann and Mookherjee, 2016). Although this new high-pressure phase with a compact 3D structure could be stable up to 35 GPa and 800 K and regarded as the potential water-carrier to transport water to the Earth's bottom transition zone and the top lower mantle, it has not been confirmed by experimental studies (Hermann and Mookherjee, 2016).

In addition to phase stability, the dehydration of brucite at high *P-T* has been an extensive research subject for years. The dehydra-

---

* Corresponding author.
*E-mail address:* zhumao@ustc.edu.cn (Z. Mao).

https://doi.org/10.1016/j.gsf.2024.101940
1674-9871/

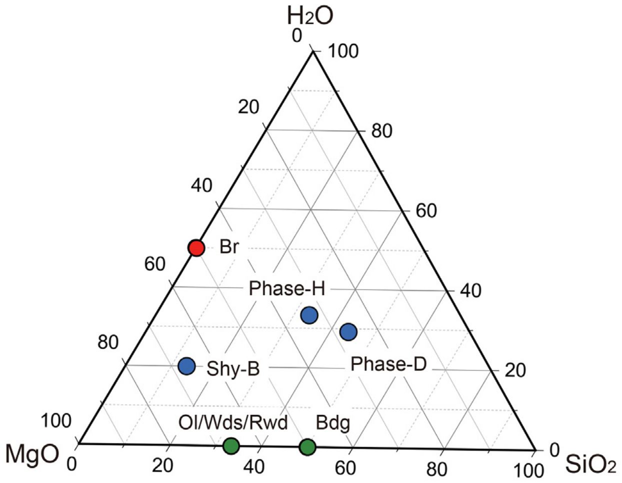

**Fig. 1.** Hydrous magnesium silicate in the $MgO$-$SiO_2$-$H_2O$ system. Br: brucite; Ol: olivine; Wds: wadsleyite; Rwd: ringwoodite; Bdg: bridgmanite; Shy-B: superhydrous Phase B.

tion temperature of brucite increases nonlinearly with pressure and reaches a maximum of ~1500 K at 10 GPa (Irving et al., 1977; Fukui et al., 2003). Elevating the pressure to 19.4 GPa leads to a decrease in the dehydration temperature of brucite to ~1320 K (Fukui et al., 2005). Although the calculated dehydration curve indicated that brucite would decompose into MgO and water–ice above 25 GPa, brucite was experimentally observed to exist up to 78 GPa/600 K and 70 GPa/750 K (Fei and Mao, 1993). Slow transformation kinetics may prevent the decomposition of brucite above 25 GPa (Fei and Mao, 1993). In the multicomponent system, brucite was experimentally observed to coexist with phase D or stishovite at 19.8–50 GPa and 1000–1250 K and was noted to be present as a minor phase to hydrous ringwoodite as diamond inclusions in mantle xenolith (Ohtani et al., 1995; Irifune et al., 1998; Ohtani et al., 2000; Nishi et al., 2014; Pearson et al., 2014). However, the dehydration of brucite above 20 GPa has not been well constrained by experimental studies.

Our study employed synchrotron X-ray diffraction (XRD) utilizing both external- and laser-heated diamond anvil cells (DACs) to investigate the phase stability of brucite at high *P-T* conditions. External heating experiments were conducted up to 29 GPa and 1150 K, while laser heating experiments covered a pressure range of 21–49 GPa at temperatures between 1100 and 1800 K. By integrating our findings with existing literature data, we determined the phase stability, density variations, and seismic velocity profiles of brucite at mantle *P-T* conditions. These insights contribute to a comprehensive understanding of brucite's fate and the dynamics of water circulation within the Earth's mantle.

## 2. Experiments

Natural single-crystal brucite from the mineral collection of the Department of Geosciences at Princeton University was used in the high *P-T* X-ray diffraction (XRD) experiments. The chemical composition of brucite, $Mg(OH)_2$, was determined by electron microprobe at the Material Center of the University of Science and Technology of China. We also performed XRD measurements under ambient conditions to confirm its crystal structure. The brucite sample used in this study is in $P\bar{3}m1$ structure, and the lattice parameters under ambient conditions were $a$ = 3.1473(7) Å and $c$ = 4.7475(12) Å, with a unit cell volume, $V_0$, of 40.72(3) Å$^3$.

Both polycrystalline and single-crystal brucite were used in high *P-T* experiments. The powder sample was grinded from a well-calibrated single-crystal brucite. For externally-heating experiments, the well-grind brucite powder was pressed into ~ 15 μm thick foils and then loaded into the externally-heated diamond anvil cells (EHDACs). Two pieces of Pt foils were placed beside the sample for pressure measurement under high *P-T*, and a ruby was also loaded near the sample for the pressure measurement during gas loading (Dewaele et al., 2006; Fei et al., 2007). For the laser-heating experiments, we mixed the powder brucite with 10 wt.% Au as the pressure calibrant and laser absorber which were then pressed into ~15 μm thick foils and loaded into the laser-heated diamond anvil cells (LHDACs) (Fei et al., 2007). The single crystals were double-side polished to ~15–20 μm in thickness. The samples were cut into 40 μm × 40 μm pieces. Two Pt foils of ~10 μm diameter were placed near the sample as the pressure calibrant, and Ne and Re were used as the pressure medium and gasket material for the high *P-T* measurements, respectively. The EHDACs were equipped with a pair of 400-μm, or 200-μm culet diamonds for experiments up to 40 GPa and 63 GPa, respectively. Heat inside the EHDACs was supplied by an alumina ceramic heater which was coiled by two 87Pt-13Rh alloy wires. The LHDACs were equipped with a pair of 300-μm culet diamonds for experiments up to 49 GPa.

We performed the high-pressure and 300 K powder XRD measurements at sector BL15U1 of Shanghai Synchrotron Radiation Facility with a wavelength of 0.6199 Å (Fig. 2). The XRD patterns

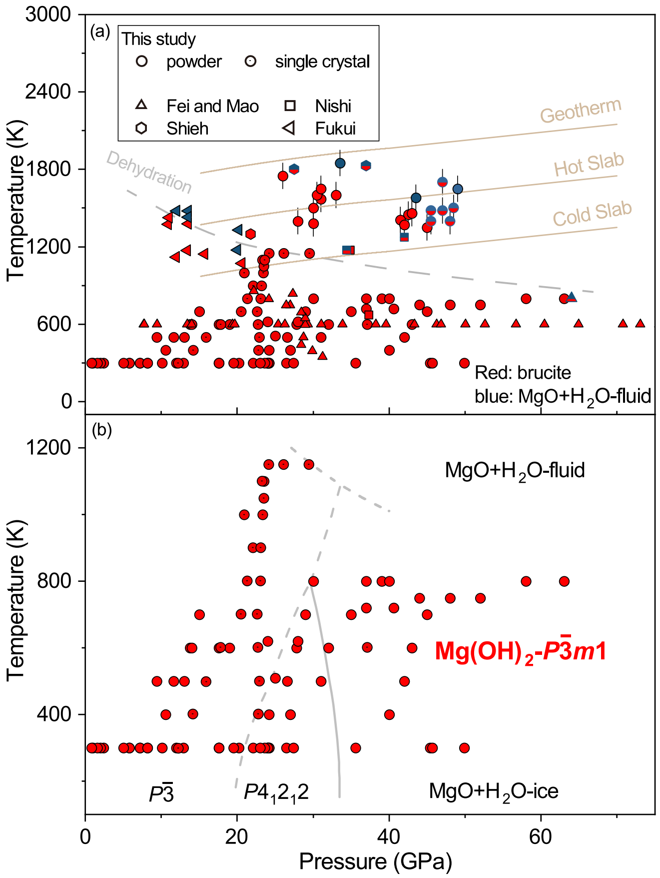

**Fig. 2.** Phase diagram of brucite at high *P-T*. (a) Phase diagram of brucite under mantle condition. Red: brucite; blue: $MgO+H_2O$. Circles: powder brucite in this study; circles with points: single-crystal brucite in this study; left triangle: Fukui et al. (2005); up triangle: Fei and Mao (1993); hexagon: Shieh et al. (1998); square: Nishi et al. (2014); brown line: geotherms in the mantle (Brown and Shankland, 1981); (b) high pressure phase diagram of brucite comparing with theoretical calculations. Circles: powder brucite in this study; circles with points: single-crystal brucite in this study; gray dashed lines: theoretical phase boundaries from Hermann and Mookherjee (2016).

were collected in the range of 2–50 GPa. The high *P-T* synchrotron XRD measurements using EHDACs were performed at both sectors 13-BMC and BMD of the Advanced Photon Source (APS) at Argonne National Laboratory (ANL). The X-ray wavelength is 0.3344 Å in BMD and 0.434 Å in BMC. The maximum experimental temperature below 30 GPa using EHDACs was 1150 K and limited to 800 K for experiments between 30 and 63 GPa. XRD patterns were collected at an interval of 50–100 K at high *P-T* conditions. The duration for heating was up to 1–2 h when the temperature was higher than 800 K. Ar with 2% hydrogen was blown into the EHDAC to avoid the oxidation of diamonds when the temperature was higher than 800 K. The LHDAC experiments between 21 and 49 GPa up to 1850 K were performed at sector 13-IDD of the APS. The used X-ray wavelength is 0.3344 Å. The pressure was calculated with the thermal EoS of Pt in EHDACs and with Au in LHDACs (Fei et al., 2007). The difference in the calculated pressure using the self-consistent pressure scale of Fei et al. (2007) between Au and Pt is within ~ 1–2 GPa in the experiment *P-T* range (Ye et al., 2017). From ~ 25 GPa, the sample was heated from both sides (upstream and downstream) using a double-sided flat top laser, and the temperature was determined by fitting the thermal radiation spectrum with the Planck radiation function under the Graybody approximation (Prakapenka et al., 2008). The XRD patterns at high *P-T* conditions were collected at every ~100 K up to 1850 K.

## 3. Results

No detectable change was identified in the XRD patterns of polycrystalline brucite in EHDACs up to 63 GPa and 800 K (Fig. 3). At 1150 K between 24 and 30 GPa, we did not observe the dehydration of single-crystal brucite by heating the sample up to 2 h (Fig. 3). During laser-heating, a complete dehydration of brucite was observed after a significant flash at 26 GPa and 1700 K and at 33 GPa and 1600 K, respectively (Fig. 2). Between 45 and 48 GPa, we observed a partial dehydration of brucite to occur at 1400 K. Before dehydration, we did not observe detectable change in the collected XRD patterns for the polycrystalline brucite compared to the pattern collected at ambient conditions (Fig. 3). Full-profile Rietveld refinement results have shown that brucite remained in the $P\bar{3}m1$ at all the investigated *P-T* conditions (Fig. 4).

XRD data from polycrystalline sample were used to determine the lattice parameters and thermal EoS of $P\bar{3}m1$ brucite (Table 1). The pressure was determined by Au and Pt (Fei et al., 2007). The obtained pressure–volume-temperature (*P-V-T*) data were fitted using the Mie-Grüneisen equations (Table 1 and Supplementary Data Fig. S1) (Jackson and Rigden, 1996). *P* is a combination pressure of the Birch-Murnaghan EoS pressure ($P_c$) at a reference temperature ($T_0$ = 300 K) and the thermal pressure ($P_{th}$):

$$P = P_c + P_{th} \tag{1}$$

Following the Birch-Murnaghan EoS, $P_c$ was derived as follows (Birch, 1938):

$$P_c = \frac{3}{2}K_{T0}\left[\left(\frac{V}{V_0}\right)^{-7/3} - \left(\frac{V}{V_0}\right)^{-5/3}\right]\cdot\left\{1 + \frac{3}{4}(K' - 4)\left[\left(\frac{V}{V_0}\right)^{-2/3} - 1\right]\right\} \tag{2}$$

where $K_{T0}$ and $V_0$ are the isothermal bulk modulus and molar volume at $P_0$ and $T_0$, respectively. The parameter $K'$ is the pressure derivative of the bulk modulus. $P_{th}$ can be written as (Jackson and Rigden, 1996):

$$P_{th}(V,T) = \frac{\gamma}{V}[(E_{th}(V,T) - E_{th}(V,T_0))] \tag{3}$$

where $E_{th}$ is the internal thermal energy between temperature $T$ and $T_0$, $\gamma$ is the Grüneisen parameter. $E_{th}$ is associated with the Debye temperature ($\theta_D$), according to Jackson and Rigden (1996):

$$E_{th}(V,T) = 9nRT\left(\frac{\theta_D}{T}\right)^{-3}\int_0^{\theta_D/T}\frac{x^3}{e^x - 1}dx \tag{4}$$

and

$$\gamma = \gamma_0\left(\frac{V}{V_0}\right)^q \tag{5}$$

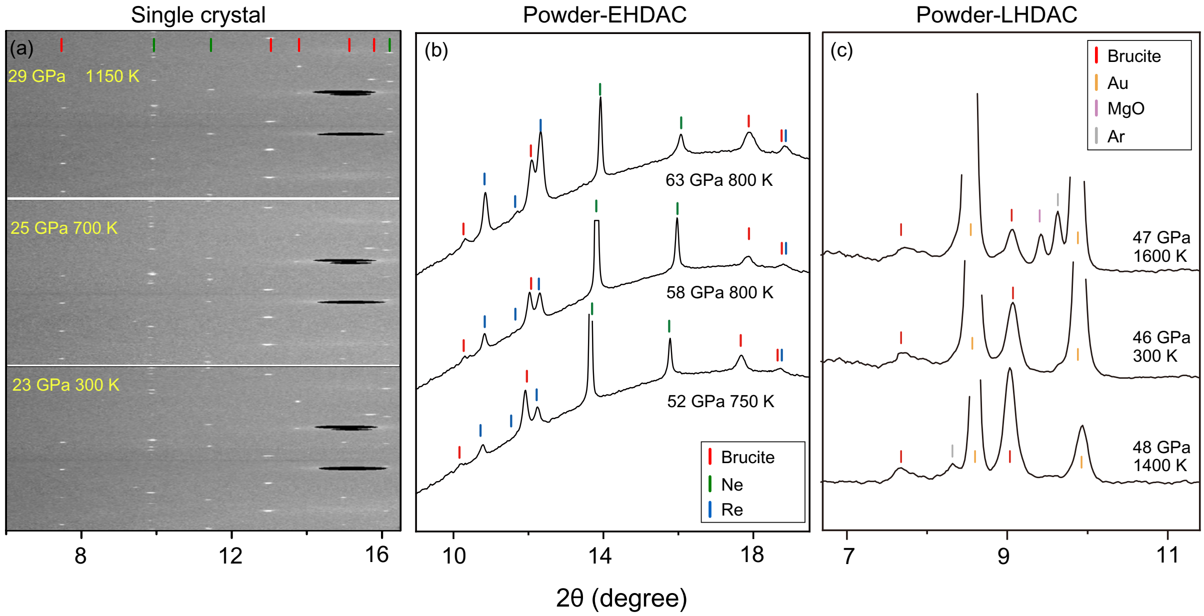

**Fig. 3.** Representative XRD patterns of brucite at high *P-T*. (a) The XRD patterns of single crystal brucite in EHDACs; (b) the XRD patterns of powder brucite in EHDACs; (c) the XRD patterns of powder brucite in LHDACs. Vertical ticks indicate the diffraction peak of different material. Red: brucite; orange: Pt; green: Ne; grey ticks: Ar; blue ticks: Re; purple ticks: MgO. The X-ray wavelength in (a) and (c) is 0.3344 Å; the X-ray wavelength in (b) is 0.434 Å.

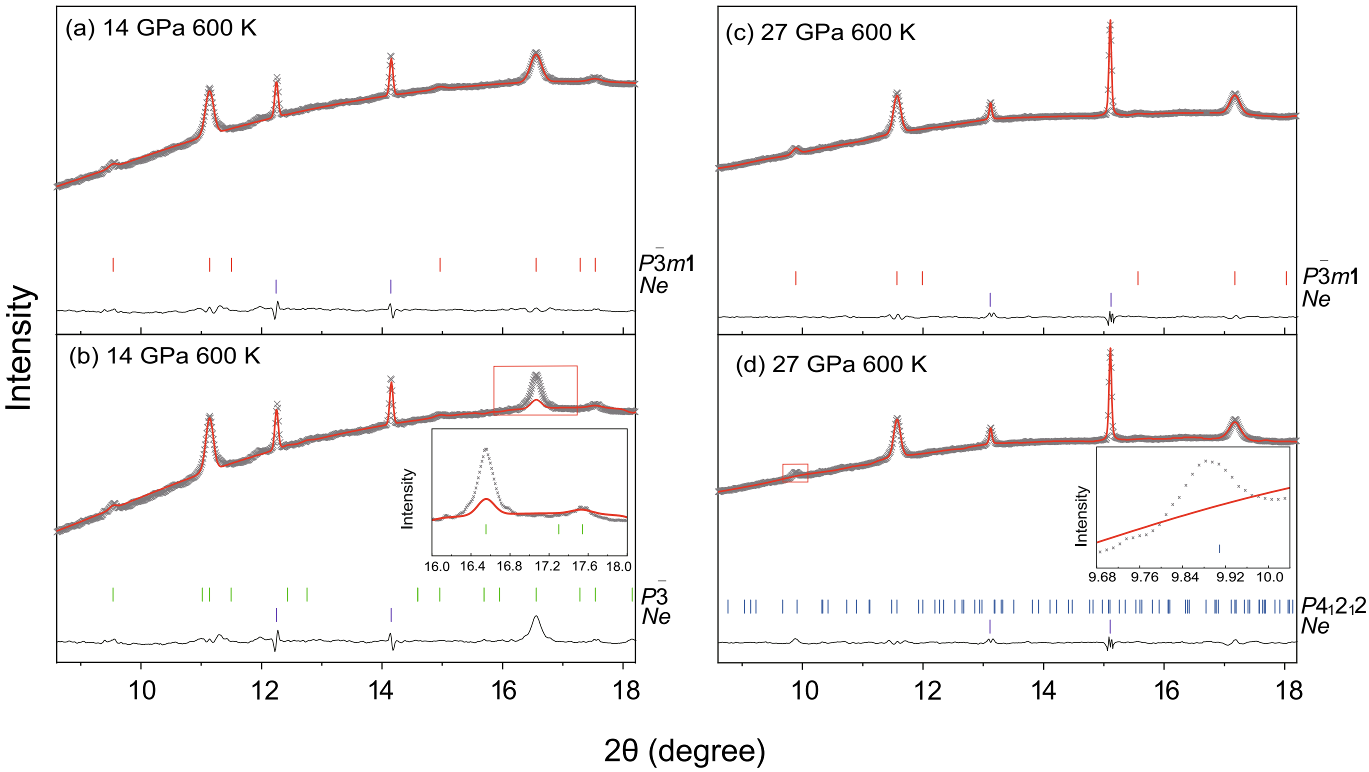

**Fig. 4.** Full-profile Rietveld refinement of the XRD patterns at representative pressure and temperature. (a, b) Refinement results at 14 GPa and 600 K with $P\bar{3}m1$ and $P\bar{3}$ structure, respectively; (c, d) refinement results at 27 GPa and 600 K with $P\bar{3}\ m1$ and $P4_12_12$ structure, respectively. Red line: refinement results; black cross: collected data. Vertical ticks indicate different minerals and or structures. Red ticks: $P\bar{3}m1$ structure brucite; green ticks: $P\bar{3}$ structure brucite; blue ticks: $P4_12_12$ structure brucite; purple ticks: Ne. The X-ray wavelength is 0.434 Å.

**Table 1**
Thermal elastic parameters of brucite in literature results.

| | $K_{T0}$ (GPa) | $K_{T0}'$ | $V_0$ (Å$^3$) | $\theta_{D0}$ (K) | $\gamma_0$ | $q$ | d$K$/d$T$ (GPa/K) | $\alpha_0$ ($10^{-5}$ /K) | $\alpha_1$ ($10^{-8}$ /K) | $P_{max}$ (GPa) | $T_{max}$ (K) |
|---|---|---|---|---|---|---|---|---|---|---|---|
| This study | 53(2) | 4.8(2) | 40.72(fixed) | 626(fixed) | 1.0(3) | 0.7(2) | | | | 48 | 1850 |
| | 56(3) | 4.5(3) | 40.72(fixed) | | | | −0.007(9) | 1.3(6) | 4.1(8) | 48 | 1850 |
| Fei and Mao (1993) | 54.3(2) | 4.7(0.2) | 40.878 | | | | −0.018(8) | 8.0(4) | | 77 | 600 |
| Fukui et al., (2003) | 41.8(1.3) | 6.6(0.3) | 40.930 | | | | −0.032(3) | 6.7 | | 23 | 873 |
| Ma et al. (2013) | 39.4(1.3) | 8.4(4) | 40.909 | | | | | | | 31 | 300 |
| Jiang et al. (2006) | 43.8(0.9) | 6.8(2) | | | | | | | | 15 | 300 |
| Xia et al. (1998) | 39.6(1.4) | 6.7(0.7) | 40.8 | | | | | | | 8 | 300 |
| Catti et al. (1995) | 39(1) | 7.6(0.7) | 40.986 | | | | | | | 11 | 300 |
| Nagai et al. (2000) | 44(1) | 6.7(fixed) | 40.746 | | | | | | | 18 | 300 |
| Duffy et al. (1995) | 42(2) | 5.7(0.5) | 40.851 | | | | | | | 20 | 300 |

where $n$ is equal to 5, which represents the number of atoms in the chemical formula of $Mg(OH)_2$, $R$ is the gas constant, $\gamma_0$ is the Grüneisen parameter under ambient conditions, and $q$ is assumed to be independent of volume (Fei et al., 1992). $\theta_D$ can be calculated as follows (Jackson and Rigden, 1996):

$$\theta_D = \theta_{D0}\exp\left(-\frac{\gamma-\gamma_0}{q}\right) \tag{6}$$

The thermoelastic parameters obtained for brucite are listed in Table 1, and fitting residuals are plotted in Supplementary Data Fig. S1. Due to the tradeoff among $\theta_{D0}$, $\gamma_0$, and $q$, these thermal parameters could not be determined individually. Here, we fixed the $\theta_{D0}$ with the value from Ye et al. (2022). To better compare our result with previous work, the high-temperature Birch-Murnaghan EoS was also used to constrain the $P$-$V$-$T$ data. The fitted $K_{T0}$, $K'$ and $V_0$ with Birch-Murnaghan EoS are listed in Table 1.

## 4. Discussion

### 4.1. Phase stability of brucite

Our experimental results provide new support for the thermal phase stability of brucite at high $P$-$T$ conditions (Fig. 2). At 800 K, brucite remains at least in the metastable state up to 63 GPa, which is consistent with previous experimental results of Fei and Mao (1993). Meanwhile, heating brucite at 1150 K between 24 and 30 GPa for two hours inside the EHDACs did not induce the decomposition (Fig. 3). When laser-heated to 43 GPa and 1500 K, we observed partial decomposition of brucite during in-situ XRD experiment. It's worth noting that the dehydration of brucite did not occur between 25 and 35 GPa up to 1800 K. The dehydration temperature observed here is greater than that in Fukui et al. (2005). The difference in dehydration temperature could be attributed to the high kinetic energy barrier during the brucite decomposition. In addition, in contrast to EHDAC experiments in which the XRD patterns were collected after two-hour heating, the heating time in LHDAC experiments is short and normally less than 10 min. The combination of high kinetic energy and limited heating time in our LHDAC experiments may impede brucite dehydration at relatively low temperatures. By combining our EHDAC results with previous large-volume press studies, we constrain the dehydration of brucite in the Earth's mantle. Brucite could enter the deep Earth with cold subduction slab and survive to the top of lower mantle.

We further examined the stable high-pressure phase of brucite using our collected XRD patterns. As mentioned above, no noticeable change was detected in our collected XRD patterns at the investigated *P-T* range before the decomposition (Fig. 3). However, a lower-trigonal symmetry structure, $P\bar{3}$, formed by the transition of protons from a dynamic positional disorder to a static positional disorder, was theoretically predicted to be more favorable than the $P\bar{3}m1$ brucite at high pressures (Mookherjee and Stixrude, 2006; Hermann and Mookherjee, 2016). We thus performed the full-profile Rietveld refinement for the XRD pattern at 15 GPa and 600 K using both $P\bar{3}m1$ and $P\bar{3}$ structure. In general, all the diffraction peaks can be well refined using the $P\bar{3}\ m1$ structure with a fitting residue as low as 6%. In contrast, the 004 peak with a $2\theta$ angle of $\sim 16.6^\circ$ (*d*-spacing 1.158 Å) cannot be refined by the $P\bar{3}$ structure, and the fitting residue using the $P\bar{3}$ structure is as large as 15%. Between 20 and 33 GPa up to 800 K, brucite was predicted to be stable in the $P4_12_12$ structure which was regarded as the potential carrier to transport water to the lower mantle (Hermann and Mookherjee, 2016). We heated the sample over 2 h and searched for the potential presence of the predicted $P4_12_12$ structure. Full-profile Rietveld refinement was also performed for the XRD pattern at 27 GPa and 600 K. However, the peak with a $2\theta$ angle of $\sim 9.8^\circ$ (*d*-spacing 1.958 Å) cannot be well-refined using the $P4_12_12$ structure. The fitting residue of the assuming $P4_12_12$ structure is 11%, much greater than 6% refined using the $P\bar{3}m1$ structure. In summary, we did not detect the phase transition of the $P\bar{3}m1$ phase to either $P\bar{3}$ or $P4_12_12$ structure in theoretical predictions (Hermann and Mookherjee, 2016). Brucite remains in the $P\bar{3}m1$ structure at the investigated *P-T* range.

### *4.2. Lattice and thermal elastic parameters of brucite*

Increasing pressure at 300 K leads to an apparent decrease in the *c/a* ratio of brucite up to 10–15 GPa (Fei and Mao, 1993; Catti et al., 1995; Duffy et al., 1995; Xia et al., 1998; Nagai et al., 2000; Fukui et al., 2003; Jiang et al., 2006; Ma et al., 2013). Yet the *c/a* ratio of brucite becomes independent of pressure upon further increasing pressure (Fig. 5). Here, our calculated *c/a* ratio at 300 K is in general agreement with most literature results up to 30 GPa (Fei and Mao, 1993; Catti et al., 1995; Duffy et al., 1995; Xia et al., 1998; Nagai et al., 2000; Fukui et al., 2003; Ma et al., 2013). The *c/a* ratio of brucite at 300 K in Fei and Mao (1993) above 10 GPa is much lower than all the other experimental results, which could be caused by no pressure medium used in their study. Our experimental results have also revealed that the increase in temperature has a minimum influence on the *c/a* ratio of brucite. In contrast, the *c/a* ratio at 600 K between 10 and 60 GPa in Fei and Mao (1993) is substantially greater than that at 300 K. As mentioned above, no pressure medium was used in Fei and Mao (1993). Elevating temperature may help reduce the deviatoric stress inside the DACs, which may contribute to the difference in the *c/a* ratio between 300 K and 600 K in Fei and Mao (1993). The *c/a* ratio appears to slightly increase with temperature in Fukui et al. (2003), although their high-temperature results seem scattered. This may be caused by the deviatoric stress inside the DAC using MgO as the pressure medium which is stiffer than Ne used in this study.

The isothermal bulk modulus, $K_{T0}$, of brucite is highly uncertain and ranges between 36 and 54 GPa with the $K'$ = 4–6.7 (Fei and Mao, 1993; Catti et al., 1995; Duffy et al., 1995; Xia et al., 1998; Nagai et al., 2000; Fukui et al., 2003; Jiang et al., 2006; Ma et al.,

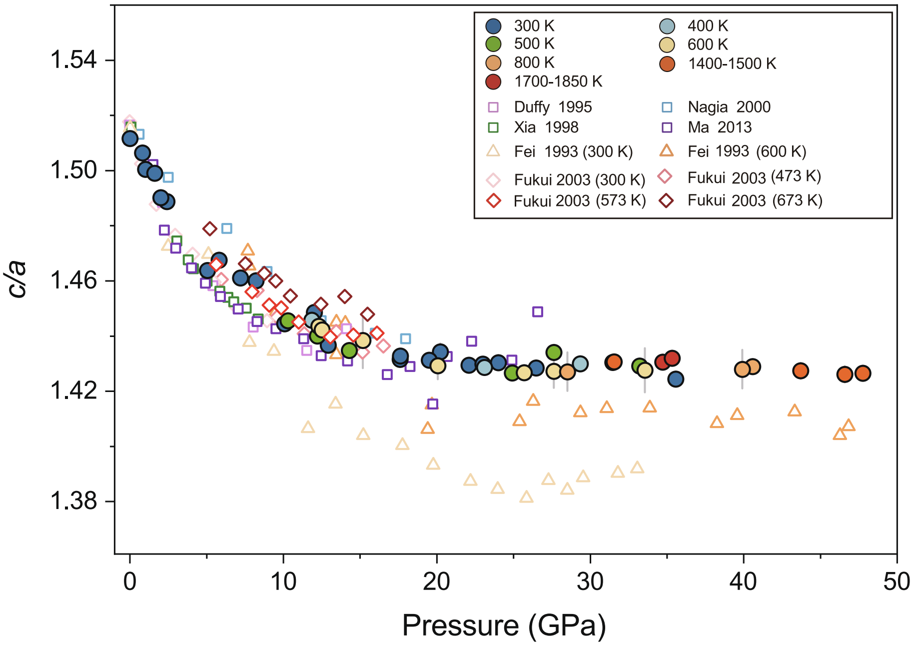

**Fig. 5.** c/a ratio of brucite at high pressures and 300 K. Solid symbol: this study; blue: 300 K; light blue: 400 K; green: 500 K; light yellow: 600 K; yellow: 800 K; orange: 1400–1500 K; red: 1700–1850 K. Open squares: high-pressure results from previous studies at 300 K; light purple: Duffy et al. (1995); green: Xia et al. (1998); blue: Nagai et al. (2000); purple: Ma et al. (2013). Light orange triangles: results from Fei and Mao (1993) at 300 K; orange triangles: results from Fei and Mao (1993) at 600 K. Light pink diamonds: results from Fukui et al. (2003) at 300 K; pink diamonds: results from Fukui et al. (2003) at 473 K; dark pink diamonds: results from Fukui et al. (2003) at 573 K; red diamonds: results from Fukui et al. (2003) at 673 K.

2013) (Supplementary Data Fig. S2). When fitting the data under 300 K, we obtained a $K_{T0}$ value of 53 GPa with $K'$ =4.8. We have noted that previous XRD experiments were mostly conducted below 30 GPa (Catti et al., 1995; Duffy et al., 1995; Nagai et al., 2000; Fukui et al., 2003; Ma et al., 2013). A narrow experimental pressure range could lead to a greater $K'$ value (Table 1) (Catti et al., 1995; Duffy et al., 1995; Nagai et al., 2000; Fukui et al., 2003; Ma et al., 2013). The $K_{T0}$ value obtained here is greater than the Voigt-Reuss-Hill average from the high-pressure Brillouin measurements at 300 K (Jiang et al., 2006). Since brucite is highly anisotropic, the Reuss and Voigt bound of brucite differ a lot. The Reuss bound of $K_{T0}$ from Brillouin measurements is 35.8 GPa with the $K'$ = 8.9, while the Voigt bound of $K_{T0}$ is 50.5 GPa with a lower $K'$ of 5.2 (Jiang et al., 2006). Our obtained $K_{T0}$ value is in a better agreement with the Voigt bound from Brillouin measurements (Jiang et al., 2006). Previous XRD measurements reported $K_{T0}$ closer to the Voigt-Reuss-Hill (VRH) average in Brillouin study (Catti et al., 1995; Duffy et al., 1995; Nagai et al., 2000; Fukui et al., 2003; Ma et al., 2013). It should be noted that brucite exhibits an anomalous change in the $a/c$ ratio above 15 GPa. Fitting our $P$-$V$ data between 1 bar and 15 GPa with a fixed $K'$=6.8 yields a $K_{T0}$ = 45(2) GPa for brucite, which was also consistent with the VRH average in Jiang et al. (2006). However, $K_{T0}$ constrained from experimental data at a much wider pressure range, like this study and Fei and Mao (1993) is closer to the Voigt bound in Jiang et al. (2006).

## 5. Geophysical implication

Up to 20% of the harzburgite layer in the subduction slabs could be altered by water to form serpentine, brucite, as well as chlorite (Hacker et al., 2003). The maximum water content in such altered harzburgite was estimated to be 2.4 wt.% (Hacker et al., 2003). Along some cold subducting slabs (700–1000 K lower than normal mantle), these harzburgites can follow the subducting slabs into the lower mantle (Kirby et al., 1996; Ganguly et al., 2009; Nishi et al., 2013; van Mierlo et al., 2013; King et al., 2015). As shown in our obtained phase diagram, brucite could remain stable along a cold slab geotherm to the topmost lower mantle and coexist with other hydrous phases in harzburgite (Ohtani et al., 1995; Kirby et al., 1996; Irifune et al., 1998; Ohtani et al., 2000; Nishi et al., 2014). Here, we have modeled the density ($\rho$) and velocity profiles ($V_P$ and $V_S$) of hydrous harzburgite with varying water content at the topmost lower mantle to decipher the seismic signature of hydrous slabs and the fate of water in the lower mantle (see Supplementary Data for details). Numerous studies have indicated that natural hydrous minerals will undergo phase transformation or decomposition into Dense Hydrous Magnesium Silicates (DHMS) under mantle conditions, and phase D is considered to be the predominant DHMS present at the top of the lower mantle (Irifune et al., 1998; Nishi et al., 2014). We thus believed that water in harzburgite is mainly stored in brucite and phase D at the topmost lower mantle in our modeling. Due to the low water storage capacity of bridgmanite (bdg) and ferropericlase (fp), we did not consider the presence of water in bdg and fp. Once the dehydration of brucite or phase D occurs, water will migrate to the overlying mantle, which will increase the volume percentage of bdg and fp in our modeling. Details in the change in mineral proportion after dehydration is in Supplementary Data.

We first calculated the density and velocity of brucite and phase D as well as lower mantle bridgmanite, ferropericlase, and davemaoite along a cold slab geotherm (Fig. 6) (Brown and Shankland, 1981). Bridgmanite and ferropericlase contain 10 and 17 mol.% Fe, respectively, and the Al content in bridgmanite is 10%. Addition of Fe leads to a linear increase in the $\rho$, bulk, and shear moduli of bridgmanite and ferropericlase at ambient conditions (see Supplementary Data) (Jacobsen et al., 2002; Marquardt et al., 2009; Yang et al., 2015; Fu et al., 2018; Fan et al., 2019). Due to a low water storage capacity of bridgmanite and ferropericlase and limited knowledge on the influence of water on the density and elasticity of these two minerals, water is only present in brucite and phase D (Dong et al., 2021). Owing to lack experimental constraints, the temperature derivative of the shear modulus ($dG/dT$) for brucite was assumed to be half of that of the bulk modulus. The pressure derivative of the shear modulus ($dG/dP$) for brucite was from a previous Brillouin study (Jiang et al., 2006).

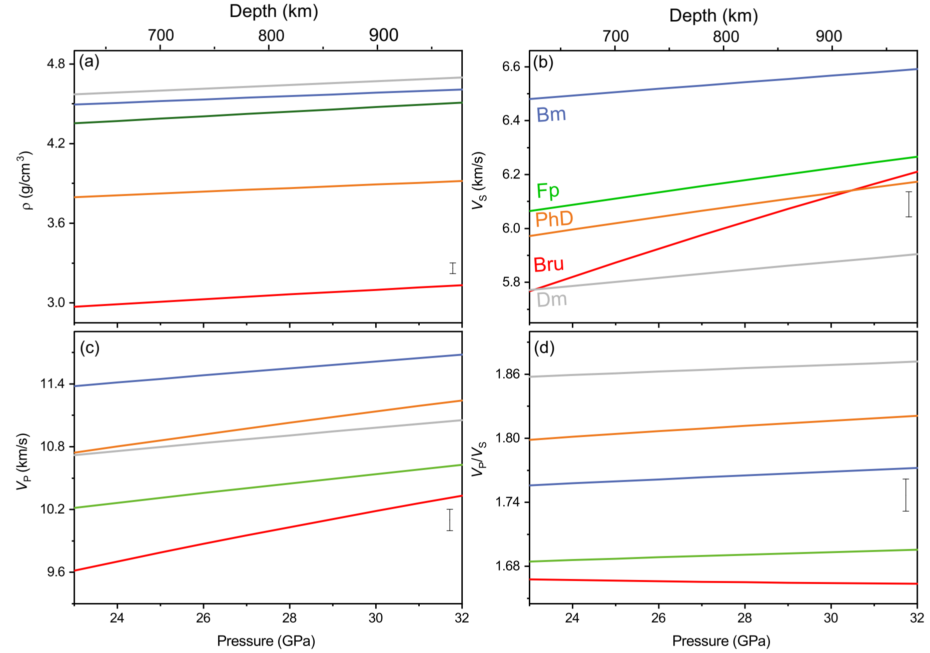

**Fig. 6.** Density and velocities of mantle minerals in the lower mantle and subducted hydrous harzburgite along slab geotherm (1000 K lower than normal mantle) (Brown and Shankland, 1981). (a) Density ($\rho$); (b) shear velocity ($V_S$); (c) compressional velocity ($V_P$); (d) $V_P/V_S$. Red lines: brucite; blue lines: bridgmanite; green lines: ferropericlase; gray lines: davemaoite; orange lines: phase D. The slab geotherm was assumed to be 1000 K lower than normal mantle (Brown and Shankland, 1981).

Along a slab geotherm 1000 K lower than the normal mantle, brucite has significantly lower $\rho$ than phase D and lower mantle minerals (Fig. 7). The density of brucite is 21(1)% lower than phase D and 31(2)%–34(2)% lower than three lower-mantle minerals at 660–900 km depth. At the top lower mantle depth, the shear-wave velocity ($V_S$) of brucite is much lower than that of phase D, bridgmanite, and ferropericlase but slightly greater than davemaoite. Due to the significant $G'$ of brucite compared to other minerals, the difference in the $V_S$ between brucite and other silicates decreases with increasing depth. At 900-km depth, although the $V_S$ of brucite is 7(1)% and 1(1)% lower than that of bridgmanite and ferropericlase, it becomes 1(1)% and 4(1)% greater than that of phase D and davemaoite, respectively. In contrast, the compressional-wave velocity ($V_P$) of brucite is 6%–17% lower than that of other silicates at 660–950 km depth.

In a multi-component assemblage, we calculated the $\rho$ and elastic moduli following (Cottaar et al., 2014):

$$\rho = \sum \rho_i V_i \tag{9}$$

where $\rho_i$ and $V_i$ are the density and volume percentage of the $i$th phase, respectively. For the bulk and shear moduli,

$$M = \frac{1}{2}\left[\sum V_i M_i + \left(\sum V_i M_i^{-1}\right)^{-1}\right] \tag{10}$$

where $M_i$ is either bulk or shear modulus of the $i$th phase. Voigt-Reuss-Hill average was applied to compute the bulk and shear moduli. $V_P$ and $V_S$ were calculated as follows:

$$V_P = \sqrt{\frac{K_S + 4G/3}{\rho}} \tag{11}$$

$$V_S = \sqrt{\frac{G}{\rho}} \tag{12}$$

where $K_S$ is the adiabatic bulk modulus, and $G$ is the shear modulus. We followed the phase diagram of Ringwood and Irifune (1988) to consider the change in phase and relative mineral proportion in harzburgite in the topmost lower mantle. The Supplementary Data (Fig. S3) shows a tradeoff in the volume proportion of brucite with phase D in harzburgite with a constant water content.

With a slab temperature 1000 K lower than the normal mantle, both density and sound velocity of dry harzburgite are greater than the surrounding mantle (Supplementary Data Fig. S4). Addition of water will lower the density and sound velocity of harzburgite. Regardless of whether water is present as phase D or brucite in harzburgite, the density of harzburgite with 1 wt.% water is almost indistinguishable from that of normal mantle considering calculation errors. Meanwhile, the velocity difference between harzburgite and the normal mantle has a weak dependence on whether water is present in phase D or brucite. When the water content in harzburgite is 1 wt.%, considering the trade-off between the contents of brucite and phase D, the brucite content can vary from 0 to 4.8% (Supplementary Data Fig. S3). In this case, the $V_S$ of the water-bearing harzburgite is 3.1(2)%–3.4(2)% faster than that of the normal mantle, and the $V_P$ is 1.7(2)%–1.8(2)% faster. At a depth of 900 km, the difference in $V_S$ between hydrous harzburgite and normal mantle slightly decreases to 2.6(3)%–2.8(3)%, while the $V_P$ difference is ~ 1.5(2)%. With a greater water content of 2.4 wt.%, density of harzburgite will be 2.2(2)%–2.8(2)% lower than the normal mantle at 660 km depth. At this depth range, the $V_P$ and $V_S$ of hydrous harzburgite are 0.3(1)%–0.7(1)% and 0.7(2)%–1.8(2)% greater than the normal mantle, respectively. Such comparison reveals that, harzburgite with 1–2.4 wt.% water, although still

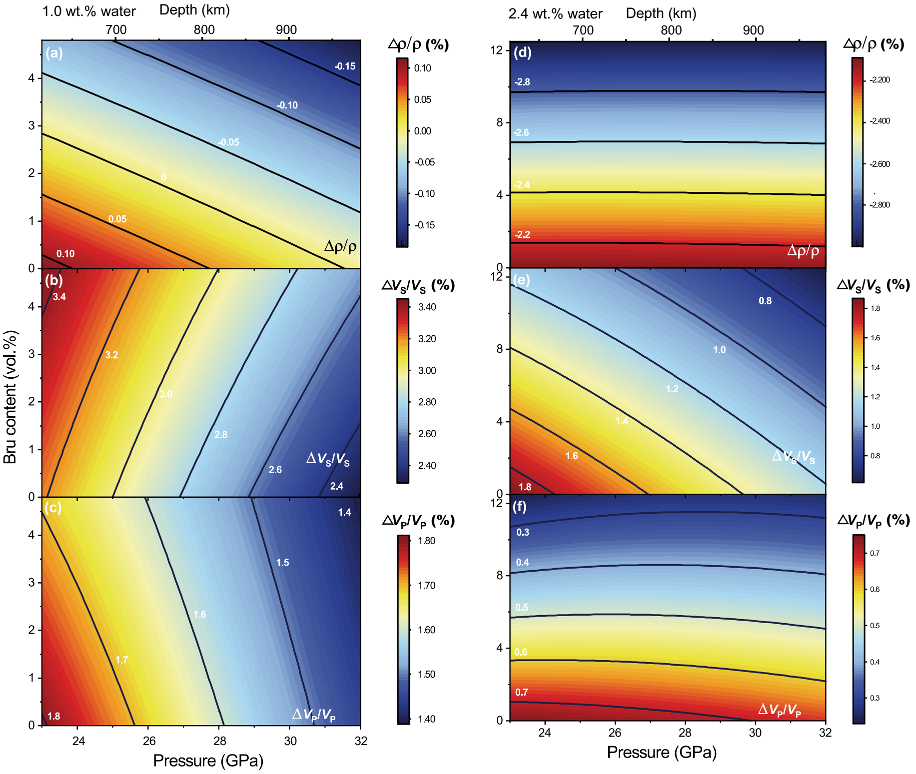

**Fig. 7.** Modelled density and velocity in subducted hydrous harzburgite under the condition of top lower mantle, with pyrolite as the reference. (a, b and c) are the $\rho$, $V_S$ and $V_P$ difference between the pyrolite model and the harzburgite model with 1.0 wt.% water. (d, e and f) are the $\rho$, $V_S$ and $V_P$ difference between the pyrolite model and the harzburgite model with 2.4 wt.% water. Pyrolite model was calculated along normal mantle geotherm, while harzburgite was modelled along a cold slab geotherm (1000 K lower than normal mantle) (Brown and Shankland, 1981). The content of brucite and phase D shared a trade off with each other as shown in Supplementary Data (Fig. S3). The average error bar in the calculation value was estimated to be 0.1%.

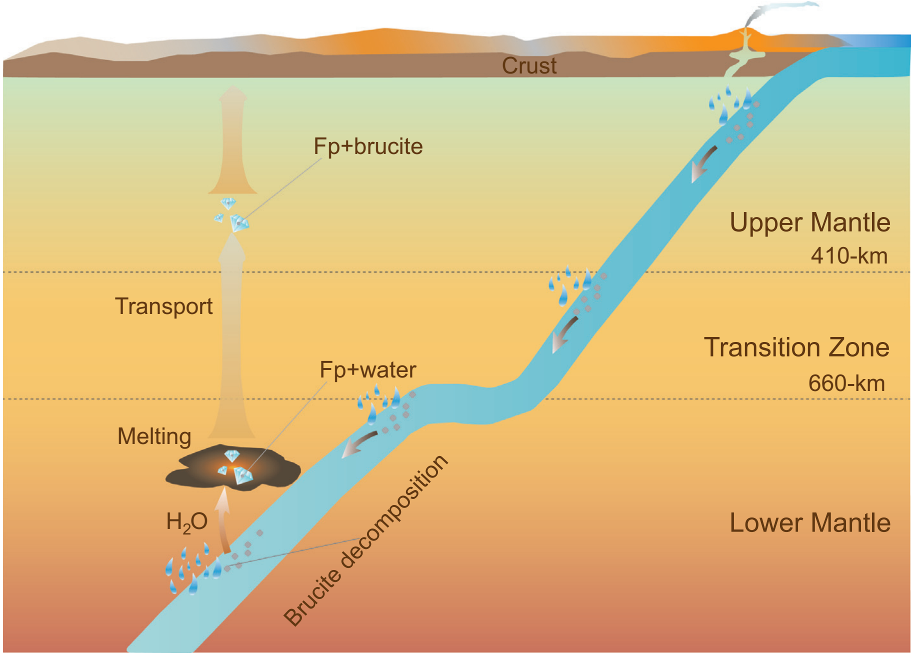

**Fig. 8.** Schematic illustration of brucite participating in the deep water cycle of the Earth. The brucite in subducted slab may survive to the 800–900 km depth. The produced water/ice from brucite would participate in the formation of diamond, and be captured as inclusion with ferropericlase (Fp). During being transported to the shallower mantle with diamond, ferropericlase may react with water and formed brucite in the inclusion again.

detectable seismologically as a high-velocity body, can decelerate the descent of the subducted slab into the lower mantle due to its density being similar to that of the normal mantle.

Meanwhile, the slab will undergo continuous heating after entering the lower mantle, causing dehydration of brucite at the depth of 800–900 km (Fig. 8). Due to the low solubility of water in lower-mantle minerals, the released water could lower the solidus of the overlying mantle and produce partial melts (Schmandt et al., 2014). These hydrous partial melts are buoyant and the desirable medium for diamond growth (Rohrbach and Schmidt, 2011). Lower-mantle ferropericlase or other lower-mantle minerals together with water released from the decomposition of brucite, could be entrapped as inclusions within diamonds which would return to the shallow depth through mantle upwelling (Tschauner et al., 2018). In the shallower mantle, water captured within diamonds will react with ferropericlase to form brucite again (Palot et al., 2016). Brucite together with other mantle minerals as diamond inclusions will finally return to the Earth's surface and complete the water circulation (Rohrbach and Schmidt, 2011).

In summary, we have studied the phase stability and thermal EoS of brucite up to 60 GPa at 800 K and 45 GPa at 1850 K. These results together with previous experimental results are useful to better constrain the dehydration condition of brucite in the Earth's mantle. More importantly, the collected XRD patterns allow us to search for the theoretically predicted new high-pressure phase of brucite high *P*-*T* conditions. However, our experimental results have shown that brucite maintains the $P\bar{3}m1$ structure throughout our investigated *P*-*T* range, and no new structure was identified. Using the obtained thermal EoS, we further discussed the influence of water on the density and velocity of subducted harzburgite in the Earth's lower mantle. In our modeling, brucite and phase D were considered as the water-bearing phases. Our modeling has revealed that both density of sound velocity of harzburgite have a weak dependence on whether water is present in phase D or brucite. Once the water content is above 1.0 wt.%, density of harzburgite will become lower than that of the normal mantle, although the sound velocity of harzburgite is still greater. A sustained increase in temperature will result in the dehydration of brucite at depths of 800–900 km. The released water could result in partial melts and contribute to the growth of deep diamonds.

## CRediT authorship contribution statement

**Ningyu Sun:** Writing – review & editing, Writing – original draft, Funding acquisition, Formal analysis, Data curation, Conceptualization. **Xinyang Li:** Writing – review & editing, Methodology, Formal analysis, Data curation. **Luo Li:** Visualization. **Qingchun Zhang:** Writing – review & editing, Formal analysis. **Yingxin Yu:** Visualization, Formal analysis. **Zhu Mao:** Writing – review & editing, Supervision, Resources, Funding acquisition, Conceptualization. **Cijin Zhou:** Formal analysis. **Dongzhou Zhang:** Writing – review & editing, Resources, Data curation.

## Acknowledgments

This work was supported by National Key R&D Program of China (2018YFA0702703), National Natural Science Foundation of China (42002036), the Strategic Priority Research Program of the Chinese Academy of Sciences (XDB18000000), and the Fundamental Research Funds for the Central Universities (WK2080000144, WK2080000189). GSECARS is supported by the National Science Foundation - Earth Sciences (EAR-1128799) and Department of Energy- GeoSciences (DE-FG02-94ER14466). APS is supported by

DOE-BES, under Contract No. DE-AC02-06CH11357. XRD data was also collected at BL15U1 of Shanghai Synchrotron Radiation Facility (proposal 2019-SSRF-PT-011379).

## Appendix A. Supplementary data

Supplementary data to this article can be found online at https://doi.org/10.1016/j.gsf.2024.101940.

## References

Birch, F., 1938. The effect of pressure upon the elastic parameters of isotropic solids, according to Murnaghan's theory of finite strain. J. Appl. Phys. 9, 279–288.

Brown, J.M., Shankland, T.J., 1981. Thermodynamic parameters in the Earth as determined from seismic profiles. Geophys. J. Roy. Astron. Soc. 66, 579–596.

Catti, M., Ferraris, G., Hull, S., Pavese, A., 1995. Static compression and H disorder in brucite, $Mg(OH)_2$, to 11 GPa: a powder neutron diffraction study. Phys. Chem. Miner. 22, 200–206.

Cottaar, S., Heister, T., Rose, I., Unterborn, C., 2014. BurnMan: A lower mantle mineral physics toolkit. Geochem. Geophy. Geosy. 15, 1164–1179.

Dewaele, A., Loubeyre, P., Occelli, F., Mezouar, M., Dorogokupets, P.I., Torrent, M., 2006. Quasihydrostatic equation of state of iron above 2 Mbar. Phys. Rev. Lett. 97, 215504.

Dong, J., Fischer, R.A., Stixrude, L.P., Lithgow-Bertelloni, C.R., 2021. Constraining the volume of Earth's early oceans with a temperature-dependent mantle water storage capacity model. AGU Adv. 2(1), e2020AV000323.

Duan, Y.F., Sun, N.Y., Wang, S.H., Li, X.Y., Guo, X., Ni, H.W., Prakapenka, V.B., Mao, Z., 2018. Phase stability and thermal equation of state of δ-AlOOH: Implication for water transportation to the Deep Lower Mantle. Earth Planet. Sci. Lett. 494, 92–98.

Duffy, T.S., Meade, C., Fei, Y.W., Mao, H.K., Hemley, R.J., 1995. High-pressure phase-transition in brucite, $Mg(OH)_2$. Am. Mineral. 80, 222–230.

Fan, D.W., Fu, S.Y., Yang, J., Tkachev, S.N., Prakapenka, V.B., Lin, J.F., 2019. Elasticity of single-crystal periclase at high pressure and temperature: The effect of iron on the elasticity and seismic parameters of ferropericlase in the lower mantle. Am. Mineral. 104, 262–275.

Fei, Y.W., Mao, H.K., 1993. Static compression of $Mg(OH)_2$ to 78 GPa at high temperature and constraints on the equation of state of fluid $H_2O$. J. Geophys. Res. 98, 11875–11884.

Fei, Y.W., Mao, H.K., Shu, J.F., Hu, J.Z., 1992. *P-V-T* equation of state of magnesiowustite $(Mg_{0.6}Fe_{0.4})O$. Phys. Chem. Miner. 18, 416–422.

Fei, Y.W., Ricolleau, A., Frank, M., Mibe, K., Shen, G.Y., Prakapenka, V., 2007. Toward an internally consistent pressure scale. PNAS 104, 9182–9186.

Fu, S., Yang, J., Zhang, Y., Okuchi, T., McCammon, C., Kim, H.-I., Lee, S.K., Lin, J.-F., 2018. Abnormal elasticity of Fe-bearing bridgmanite in the Earth's lower mantle. Geophys. Res. Lett. 45, 4725–4732.

Fukui, H., Ohtaka, O., Suzuki, T., Funakoshi, K., 2003. Thermal expansion of $Mg(OH)_2$ brucite under high pressure and pressure dependence of entropy. Phys. Chem. Miner. 30, 511–516.

Fukui, H., Inoue, T., Yasui, T., Katsura, T., Funakoshi, K., Ohtaka, O., 2005. Decomposition of brucite up to 20 GPa: evidence for high MgO-solubility in the liquid phase. Eur. J. Mineral. 17, 261–267.

Ganguly, J., Freed, A.M., Saxena, S.K., 2009. Density profiles of oceanic slabs and surrounding mantle: Integrated thermodynamic and thermal modeling, and implications for the fate of slabs at the 660 km discontinuity. Phys. Earth Planet. Int. 172, 257–267.

Guo, X.Z., 2016. Experimental study of the electrical conductivity of hydrous minerals in the crust and the mantle under high pressure and high temperature. Sci. China Earth Sci. 59, 696–706.

Hacker, B.R., Abers, G.A., Peacock, S.M., 2003. Subduction factory - 1. Theoretical mineralogy, densities, seismic wave speeds, and $H_2O$ contents. J. Geophys. Res. 108.

Hermann, A., Mookherjee, M., 2016. High-pressure phase of brucite stable at Earth's mantle transition zone and lower mantle conditions. PNAS 113, 13971–13976.

Irifune, T., Kubo, N., Isshiki, M., Yamasaki, Y., 1998. Phase transformations in serpentine and transportation of water into the lower mantle. Geophys. Res. Lett. 25, 203–206.

Irving, A.J., Huang, W.L., Wyllie, P.J., 1977. Phase relations of portlandite, $Ca(OH)_2$ and brucite, $Mg(OH)_2$ to 33 kilobars. Am. J. Sci. 277, 313–321.

Jackson, I., Rigden, S.M., 1996. Analysis of P-V-T data: Constraints on the thermoelastic properties of high-pressure minerals. Phys. Earth Planet. Int. 96, 85–112.

Jacobsen, S.D., Reichmann, H.J., Spetzler, H.A., Mackwell, S.J., Smyth, J.R., Angel, R.J., McCammon, C.A., 2002. Structure and elasticity of single-crystal (Mg, Fe)O and a new method of generating shear waves for gigahertz ultrasonic interferometry. J. Geophys. Res. 107. https://doi.org/10.1029/2001JB000490.

Jiang, F.M., Speziale, S., Duffy, T.S., 2006. Single-crystal elasticity of brucite, $Mg(OH)_2$, to 15 GPa by Brillouin scattering. Am. Mineral. 91, 1893–1900.

King, S.D., Frost, D.J., Rubie, D.C., 2015. Why cold slabs stagnate in the transition zone. Geology 43, 231–234.

Kirby, S.H., Stein, S., Okal, E.A., Rubie, D.C., 1996. Metastable mantle phase transformations and deep earthquakes in subducting oceanic lithosphere. Rev. Geophys. 34, 261–306.

Li, X.Y., Mao, Z., Sun, N.Y., Liao, Y.F., Zhai, S.M., Wang, Y., Ni, H.W., Wang, J.Y., Tkachev, S.N., Lin, J.F., 2016. Elasticity of single-crystal superhydrous phase B at simultaneous high pressure-temperature conditions. Geophys. Res. Lett. 43, 8458–8465.

Litasov, K.D., Ohtani, E., Ghosh, S., Nishihara, Y., Suzuki, A., Funakoshi, K., 2007. Thermal equation of state of superhydrous phase B to 27 GPa and 1373 K. Phys. Earth Planet. Int. 164, 142–160.

Litasov, K.D., Ohtani, E., Nishihara, Y., Suzuki, A., Funakoshi, K., 2008. Thermal equation of state of Al- and Fe-bearing phase D. J. Geophys. Res. 113. https://doi.org/10.1029/2007jb004937.

Liu, J., Hu, Q.Y., Bi, W.L., Yang, L.X., Xiao, Y.M., Chow, P., Meng, Y., Prakapenka, V.B., Mao, H.K., Mao, W.L., 2019. Altered chemistry of oxygen and iron under deep Earth conditions. Nat. Commun. 10 (1), 153.

Ma, M.N., Liu, W., Chen, Z.Q., Liu, Z.X., Li, B.S., 2013. Compression and structure of brucite to 31 GPa from synchrotron X-ray diffraction and infrared spectroscopy studies. Am. Mineral. 98, 33–40.

Marquardt, H., Speziale, S., Reichmann, H.J., Frost, D.J., Schilling, F.R., 2009. Single-crystal elasticity of $(Mg_{0.9}Fe_{0.1})O$ to 81 GPa. Earth Planet. Sci. Lett. 287, 345–352.

Mookherjee, M., Stixrude, L., 2006. High-pressure proton disorder in brucite. Am. Mineral. 91, 127–134.

Nagai, T., Hattori, T., Yamanaka, T., 2000. Compression mechanism of brucite: An investigation by structural refinement under pressure. Am. Mineral. 85, 760–764.

Nishi, M., Kubo, T., Ohfuji, H., Kato, T., Nishihara, Y., Irifune, T., 2013. Slow Si–Al interdiffusion in garnet and stagnation of subducting slabs. Earth Planet. Sci. Lett. 361, 44–49.

Nishi, M., Irifune, T., Tsuchiya, J., Tange, Y., Nishihara, Y., Fujino, K., Higo, Y., 2014. Stability of hydrous silicate at high pressures and water transport to the deep lower mantle. Nat. Geosci. 7, 224–227.

Ohtani, E., 2020. The role of water in Earth's mantle. Nat. Sci. Rev. 7, 224–232.

Ohtani, E., Shibata, T., Kubo, T., Kato, T., 1995. Stability of hydrous phases in the transition zone and the upper most part of the lower mantle. Geophys. Res. Lett 22, 2553–2556.

Ohtani, E., Mizobata, H., Yurimoto, H., 2000. Stability of dense hydrous magnesium silicate phases in the systems $Mg_2SiO_4$-$H_2O$ and $MgSiO_3$-$H_2O$ at pressures up to 27 GPa. Phys. Chem. Miner. 27, 533–544.

Palot, M., Jacobsen, S.D., Townsend, J.P., Nestola, F., Marquardt, K., Miyajima, N., Harris, J.W., Stachel, T., McCammon, C.A., Pearson, D.G., 2016. Evidence for $H_2O$-bearing fluids in the lower mantle from diamond inclusion. Lithos 265, 237–243.

Pearson, D.G., Brenker, F.E., Nestola, F., McNeill, J., Nasdala, L., Hutchison, M.T., Matveev, S., Mather, K., Silversmit, G., Schmitz, S., Vekemans, B., Vincze, L., 2014. Hydrous mantle transition zone indicated by ringwoodite included within diamond. Nature 507, 221–224.

Piet, H., Leinenweber, K.D., Tappan, J., Greenberg, E., Prakapenka, V.B., Buseck, P.R., Shim, S.-H., 2020. Dehydration of δ-AlOOH in Earth's deep lower mantle. Minerals 10, 384.

Prakapenka, V.B., Kubo, A., Kuznetsov, A., Laskin, A., Shkurikhin, O., Dera, P., Rivers, M.L., Sutton, S.R., 2008. Advanced flat top laser heating system for high pressure research at GSECARS: Application to the melting behavior of germanium. High Press. Res. 28, 225–235.

Ringwood, A., Irifune, T., 1988. Nature of the 650–km seismic discontinuity: implications for mantle dynamics and differentiation. Nature 331, 131–136.

Rohrbach, A., Schmidt, M.W., 2011. Redox freezing and melting in the Earth's deep mantle resulting from carbon-iron redox coupling. Nature 472, 209–212.

Schmandt, B., Jacobsen, S.D., Becker, T.W., Liu, Z., Dueker, K.G., 2014. Dehydration melting at the top of the lower mantle. Science 344, 1265–1268.

Shieh, S.R., Mao, H.K., Hemley, R.J., Ming, L.C., 1998. Decomposition of phase D in the lower mantle and the fate of dense hydrous silicates in subducting slabs. Earth Planet. Sci. Lett. 159 (1–2), 13–23. https://doi.org/10.1016/S0012-821X(98)00062-4.

Tschauner, O., Huang, S., Greenberg, E., Prakapenka, V.B., Ma, C., Rossman, G.R., Shen, A.H., Zhang, D., Newville, M., Lanzirotti, A., Tait, K., 2018. Ice-VII inclusions in diamonds: Evidence for aqueous fluid in Earth's deep mantle. Science 359, 1136–1139.

van Mierlo, W.L., Langenhorst, F., Frost, D.J., Rubie, D.C., 2013. Stagnation of subducting slabs in the transition zone due to slow diffusion in majoritic garnet. Nat. Geosci. 6, 400–403.

Walter, M.J., Thomson, A.R., Wang, W., Lord, O.T., Ross, J., McMahon, S.C., Baron, M. A., Melekhova, E., Kleppe, A.K., Kohn, S.C., 2015. The stability of hydrous silicates in Earth's lower mantle: Experimental constraints from the systems $MgO$-$SiO_2$-$H_2O$ and $MgO$-$Al_2O_3$-$SiO_2$-$H_2O$. Chem. Geol. 418, 16–29.

Xia, X., Weidner, D.J., Zhao, H., 1998. Equation of state of brucite: Single-crystal Brillouin spectroscopy study and polycrystalline pressure-volume-temperature measurement. Am. Mineral. 83, 68–74.

Yang, J., Tong, X.Y., Lin, J.F., Okuchi, T., Tomioka, N., 2015. Elasticity of ferropericlase across the spin crossover in the Earth's lower mantle. Sci. Rep. 5, 17188.

Ye, Y., Prakapenka, V., Meng, Y., Shim, S.H., 2017. Intercomparison of the gold, platinum, and MgO pressure scales up to 140 GPa and 2500 K. J. Geophys. Res.-Sol. Ea. 122, 3450–3464.

Ye, Y., Smyth, J.R., Chen, G., 2022. Hydration effect on equations of state for minerals in the peridotite system: Implication for geotherms in the mantle. J. Earth Sci. 33, 1124–1144.